



Magnetite trace element characteristics and their use as a proximity indicator to the Avoca Tank Cu-Au prospect, Girilambone copper province, New South Wales, Australia

Brenainn Simpson¹ · Joel Fitzherbert¹ · Jake Moltzen¹ · Ian Baillie² · Brad Cox² · Huiqing Huang³

Received: 4 June 2021 / Accepted: 9 August 2023 / Published online: 1 September 2023
© Crown 2023

Abstract

The Avoca Tank orebody is one of a series of copper-rich orebodies occurring within the Girilambone Cu province of central New South Wales. Mineralisation at Avoca Tank is hosted within several narrow, chloritic, greenschist-facies shear zones which developed ~430 Ma (U-Pb titanite) within metasedimentary rocks around the margins of an Ordovician (ca. 470 Ma) mafic sill complex. Mineralisation at Avoca Tank preserves an early oxide phase (sulfide barren) as magnetite-rich shears that are overprinted by a pyrite-chalcopyrite-rich sulfide phase. The mineralogical and chemical footprint surrounding sulfide mineralisation is narrow (<50 m) offering limited ore vectoring using mineralogical and chemical change. However, magnetite-rich shears occur external to and within sulfide mineralised intervals, and magnetite within these shears displays distinctive trace element variation depending on proximity to Cu mineralisation. Changing magnetite trace element chemistry with increasing Cu abundance at Avoca Tank is best represented by two ternary systems. A ternary plot of Ni-V-Ti effectively separates magnetite from unmineralised zones via Ni abundance, while the ratio of Ti to V effectively separates magnetite from low-, moderate- and high-grade Cu zones. A ternary plot of Sn (100*Sn)-Zn-Ni effectively discriminates between unmineralised, low-grade and combined moderate- to high-grade zones. The greatest control here is the ratio of Zn to Sn, but the inclusion of Ni abundance provides a greater separation between low- versus combined high- and moderate-grade ore. Many of the trace element trends recorded in magnetite are mirrored in the overprinting sulfides. We propose a two-phase mineralising system, with initial development of chemically uniform, sulfide barren magnetite-chlorite-rich shear zones in proximity to the margins of older mafic sills. A subsequent, and potentially hotter (+60 °C), fluid harvested the early oxide for Fe, with the partial replacement, recrystallisation and re-equilibration magnetite within a sulfide-rich hydrothermal fluid under greenschist facies metamorphic conditions. As many known orebodies in the Girilambone Cu province are associated with magnetite-rich gangue, magnetic surveys are an effective exploration technique. Based on this pilot study, mapping trace element variation in magnetite within these bodies is an additional ore-vectoring technique in the search for economic Cu mineralisation in this province.

Keywords Girilambone · Magnetite · Proximity indicator · Trace element · Orebody discriminator

Introduction

Ore deposit discriminators have been increasingly used in recent decades to constrain both the style of mineralisation and the origins of mineralising fluids (Brugger et al. 2000; Dupuis and Beaudoin 2011; Nadoll 2011; Nadoll et al. 2014; Dare et al. 2014; O'Brien et al. 2015; Mao et al. 2016; Evans 2017; Wilkinson et al. 2020). This is achieved by observing common geochemical characteristics in minerals from various deposit styles which are resistant to sub-solidus modification, then using this data to create discrimination diagrams. Many such resistate indicator minerals (RIMs) have been used to

Editorial handling: Z. Chang

✉ Brenainn Simpson
brenainn.simpson@regional.nsw.gov.au

¹ Geological Survey of New South Wales, Maitland, Australia

² Aeris Resources, Brisbane, Australia

³ James Cook University, Townsville, Australia

fingerprint different deposit types, including rutile, chromite, tourmaline, garnet, magnetite, apatite, scheelite and titanite. The usefulness of a RIM is dependent on a pervasive occurrence within the orebody, the ability to substitute a variety of trace elements which can be used to infer compositional characteristics of the ore forming fluid, an ability to resist re-equilibration, weathering and transport, and a relative ease of separation and analysis (Poulin et al. 2018).

The Avoca Tank Cu deposit is host to early-stage magnetite that has been subsequently overprinted by pyrite and chalcopyrite. The small alteration footprint of the deposit (<50 m) means that sulfide mineralisation and related alteration are difficult to intercept in drill core. Here, magnetite is an ideal RIM due to a widespread occurrence within shear zones distal to the orebody as well as its ubiquitous occurrence throughout the orebody. Additionally, magnetite is easily observed petrographically providing constraints on the nature and paragenesis of the RIM as proximity to the orebody increases. Magnetite at Avoca Tank has been affected by re-equilibration and demonstrates consistent variation in trace element concentrations between unmineralised shear zones and zones of high-grade Cu mineralisation.

A wide variety of elements substitute into magnetite and consequently form solid solutions with other spinel group minerals (Dupuis and Beaudoin 2011; Nadoll 2011; Nadoll et al. 2014; Dare et al. 2014). The main discriminator elements in magnetite are Mg, Al, Ti, V, Cr, Mn, Co, Ni, Zn and Ga (Nadoll et al. 2014), and chemical variation within the magnetite and other minerals that have crystallised in equilibrium is driven by the available metal budget of the crystallising fluid, with consideration given to fluid mixing and fluid-wall rock interactions, temperature and oxygen fugacity (Carew et al. 2006). Thus, geochemical analyses of magnetite provide insight into the character of the fluids in a deposit where magnetite is paragenetically related to the ore forming event. The ability to measure these elements with high precision using a laser ablation inductively coupled plasma mass spectrometer (LA-ICP-MS) has been a chief driver in the high interest in magnetite as an ore deposit discriminator and proximity indicator (Grigsby 1990; Dare et al. 2012, 2014; Nadoll et al. 2014).

Magnetite is a stable phase at a range of temperatures and pressures and is a common gangue mineral in many styles of ore deposits, as well as in igneous, metamorphic, metasomatic and sedimentary rocks. Magnetite from different geological settings can be demonstrated to have different geochemical characteristics in metamorphic (Hall and Fisher 1987; Grant 1985), metasomatic (Heimann et al. 2005; Zhao et al. 2019) and sedimentary rocks (Grigsby 1990; Razjigaeva and Naumova 1992; Yang et al. 2009). The same is true of many mineral systems, including volcanogenic massive sulfide (Heimann et al. 2005), iron oxide copper gold and iron oxide apatite (Carew et al. 2006; Knipping et al. 2015; Huang et al.

2019a), banded iron formation (Maskell et al. 2014; Gourcerol et al. 2016), porphyry (Mavrogenatos et al. 2019; Huang et al. 2019b), skarn (Wang et al. 2018a, 2018b), Ni-Cu-PGE deposits (Boutroy et al. 2014; Jiao et al. 2019), hydrothermal systems (Nadoll et al. 2014) and other less constrained deposits (López-García et al. 2017; Valvasori et al. 2020; Wang et al. 2020; Spry et al. 2015). Trace element geochemistry of hydrothermal magnetite and other minerals can be used to provide a vector towards an orebody in porphyry systems (Cooke et al. 2017; Wilkinson et al. 2020) and has been used as a detrital mineral vector in glacial terranes (Makvandi et al. 2013; Pisiak et al. 2017).

In this study, we utilise trace element geochemical analyses of magnetite, pyrite, chalcopyrite and siderite to indicate proximity to Cu grade at Avoca Tank. This is achieved in conjunction with petrographic characterisation, whole rock geochemistry and hyperspectral data to constrain the paragenesis of the ore-forming event and the nature of the alteration halo at Avoca Tank. Previous workers (Dupuis and Beaudoin 2011; Nadoll et al. 2014) have utilised magnetite in a similar way and have presented various ore deposit discrimination diagrams for the purpose of determining deposit style and formation conditions. These diagrams were tested to determine their efficacy in predicting the mineralisation style of the Avoca Tank Cu deposit.

Geological context

The Girilambone Cu province is hosted in the Narrama Formation of the Girilambone Group, a sequence of Ordovician quartzose turbidite interbedded/intercalated with minor chert, quartzite, thick quartzose sandstone, arkosic submarine debris flows, and basaltic sills and flows associated with interpreted quartz Fe-oxide-rich exhalative units (Burton et al. 2012; Gilmore et al. 2018). The Narrama Formation was deposited during the Early Ordovician (485–470 Ma) as deep water turbidites associated with basaltic magmatism (both MORB and IOB affinities; Burton 2011) in a back-arc environment (Glen et al. 2007). Within the Narrama Formation, mineralisation occurs stratigraphically below the Budgery Sandstone Member, a mature coarse-grained quartzite package used as a marker bed within the terrane (Hinde 2019). Cu mineralisation is spatially associated with mafic units that display MORB affinities (Burton 2011) and both Cu mineralisation and the mafic volcanics occur within a regionally extensive, stratabound belt (Fig. 1). Girilambone Cu deposits are typically classified as Besshi type (mafic-pelitic VMS) and likely formed in association with mafic magmatism during Early Ordovician back arc extension (Suppel 1975; Jones 2012; Gilmore et al. 2018; Fergusson and Henderson 2015; Downes et al. 2017).

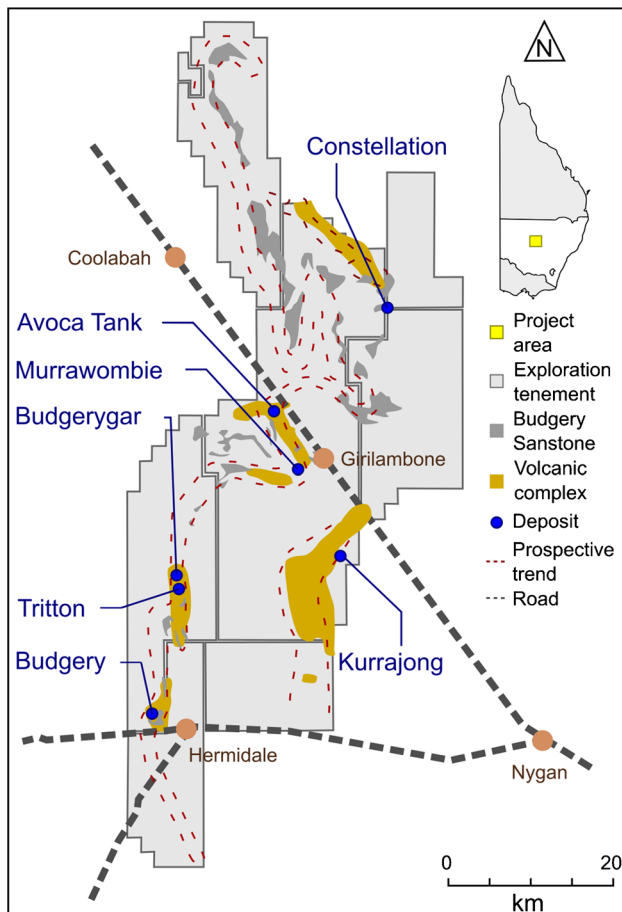


Fig. 1 Simplified geological map of the Girilambone Cu province. Figure depicts the main deposits and prospects and the association with regional belt of mafic volcanic complexes. Mineralisation occurs stratigraphically below the Budgery Sandstone Member which is used as a marker bed for exploration in the area

The Girilambone Group underwent compressional deformation and greenschist facies metamorphism during the Late Ordovician to early Silurian Benambran Orogeny (490–435 Ma). The Benambran Orogeny was followed by orogenic collapse and widespread extensional tectonism associated with the development of successor back arc basin systems during the Siluro-Devonian between 430 and 410 Ma (e.g. Cobar Basin further west, Fitzherbert and Downes 2020). The region underwent renewed compression during the Late Devonian Tabberabberan Orogeny (390–380 Ma). While the Girilambone Group Cu deposits are epigenetic, they are interpreted to be remobilised Cu derived from fertile basement, potentially Early Ordovician back arc systems (Stegman 2001; Lawrie and Hinman 1998). Ore remobilisation has also been suggested from Devonian Pb model ages obtained from sulfides at Tritton Cu mine, the largest of the interpreted Besshi systems in the province (Huston et al. 2016). Gilmore (2014) suggested that pyrite from the nearby Tritton orebody had chemical characteristics consistent with

a mafic VMS mineralisation system. The Avoca Tank orebody displays a strong structural control and may potentially have formed through chemical remobilisation of Besshi ore, forming epigenetic ore relationships or as new mineralisation during subsequent deformation and (or) metamorphism of the Cu-fertile Early Ordovician back arc sequences.

Characteristics of the Avoca Tank deposit

The Avoca Tank orebody is a relatively small high-grade deposit (0.7 mt at 2.5% Cu and 0.8 g/t Au), in comparison to the nearby Tritton orebody but has higher Cu, Zn, Ag and Au grades. The deposit is hosted in psammitic to pelitic metasedimentary rocks interlayered with dolerite sills and underlying a coarse-grained sandstone hanging wall sequence. Mineralisation occurs as narrow shear-hosted massive magnetite-pyrite-chalcopyrite-sphalerite ± pyrrhotite forming elongated, flattened pipe-like bodies.

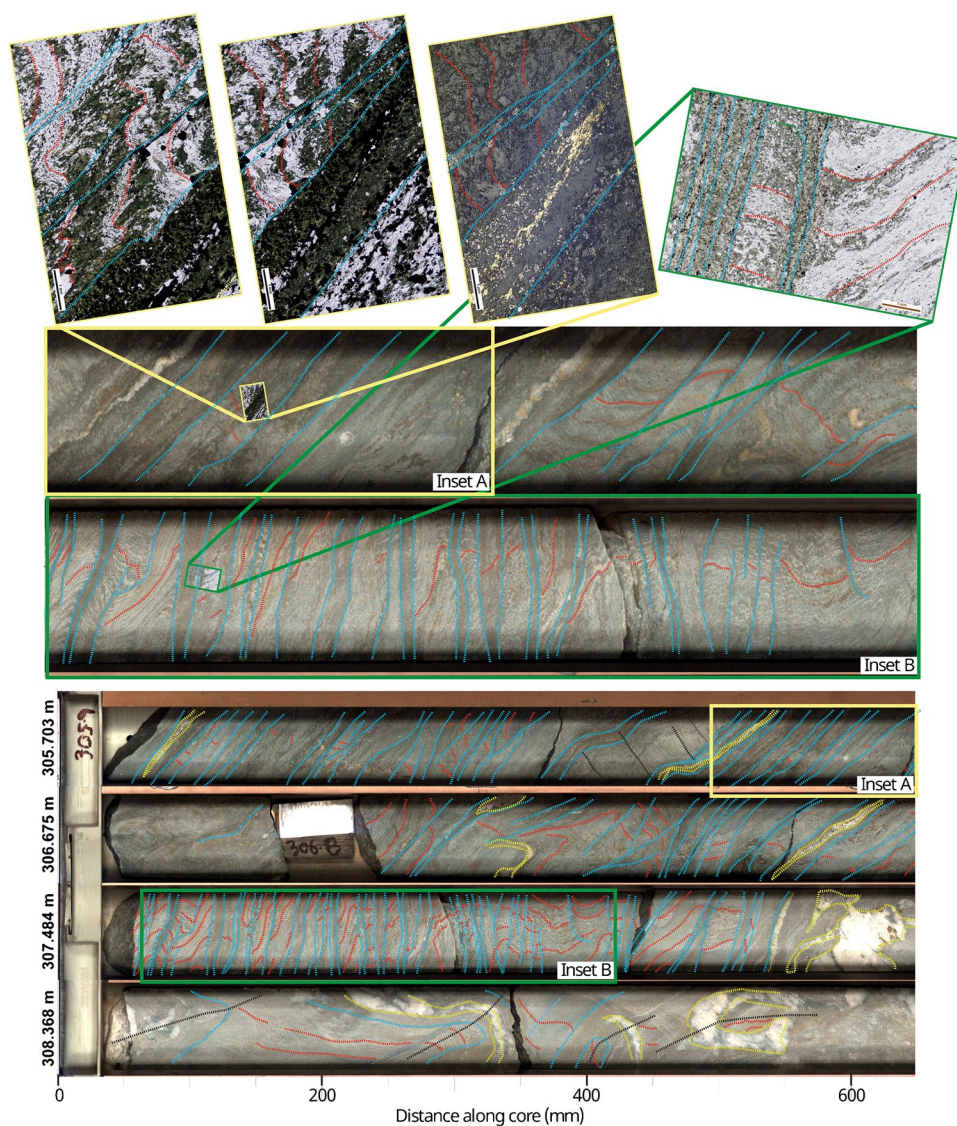
Host rocks

The host sequence is dominated by variably foliated medium- to thick-bedded, medium-grained metasandstone of the Narrama Formation. Metasandstone typically displays a bimodal grainsize distribution with ~0.5–1 mm quartz and albite grains set in a fine-grained, often recrystallised quartz-rich matrix. Individual beds display well developed grading. White mica ± chlorite typically occurs in characteristic closely spaced, foliated lamellae that have been interpreted as an evolved spaced crenulation cleavage or differentiated layering. Interbedded, fine-grained pelitic schist typically displays a continuous cleavage defined by white mica and chlorite. Metadolerite sills are generally metres to decametres in thickness with doleritic textures preserved in the core of the sills and strongly foliated margins. The sills typically comprise chlorite-albite-actinolite-epidote-titanite-carbonate reflecting the complete recrystallisation of their primary mineralogy during metamorphism and hydrothermal alteration. Consequently, the sills have a low magnetic susceptibility and are not distinguished easily via geophysical methods.

Structural chronology

The structural chronology at Avoca Tank is consistently logged in drill core and has been well described by Murphy and Cox (2019) for Avoca Tank, as well as for the Murrawombie and Tritton deposits in the region. The most prominent fabric is S_2 , a closely spaced, bedding parallel cleavage often expressed as a well-developed differentiated layering in metasandstone horizons (Fig. 2). Although not observed during this study, previous workers have described a poorly preserved foliation (S_1) that is overprinted by the S_2

Fig. 2 Structural interpretation of narrow mineralised shear zones from drill hole TATD043 from approximately 306–309 m down hole (red lines = S₂ spaced cleavage orientation, blue lines = D₃ shear boundaries, yellow lines = D₃ quartz-carbonate veins, black lines = F₄ fold axes). Insets A and B are closeup images of the core that was sampled for petrographic analysis. Photomicrographs of the sample locations are included to illustrate the relationship of the mineralised D₃ shears with the earlier S₂ foliation



fabric (Fergusson and Henderson 2015). S₂ is expressed as a continuous slaty to fine-grained schistose cleavage in pelitic horizons and is crosscut by a more widely spaced array of D₃ shears (Fig. 2). D₃ shears are typically developed at a high angle to S₂, being characteristically narrow external to the mineralised interval, and becoming noticeably wider and more closely spaced as mineralisation is approached (Fig. 2). Closely spaced D₃ shear arrays can locally resemble S₂ within the mineralised interval. Importantly, mineralisation at Avoca Tank is only observed within these D₃ shear zones, although foliation parting parallel to S₂ has locally facilitated mineralisation parallel to S₂/bedding, often within hinge zones; a mechanism akin to the formation of saddle reefs. Chloritic or carbonate alteration may also invade the host rock in foliation parallel zones for a short distance away from the mineralised shears. The orientation of D₃ shears is remarkably uniform, at a low angle to drill core axis with a

consistent normal shear sense (Fig. 2). While drag folding of S₂ is prominent around the margins of the D₃ shears, the D₃ shear zones are characteristically displayed weak internal deformation, although brecciation foliation development parallel to S₃ is locally observed. D₄ folds locally rotate the S₂ foliation and D₃ shear zones, being particularly prominent where refolding D₃ quartz carbonate veins (Fig. 2; Murphy and Cox 2019). Peripheral to the mineralised interval D₄ folds are open with a weak, spaced axial planar foliation. D₄ strain is locally higher within the mineralised interval and may be responsible for tight to isoclinal folding of S₃ within wide chloritic D₄ shear zones. Chalcopyrite may be remobilised into higher strain D₄ shear zones.

Fergusson and Henderson (2015) reported muscovite and whole rock Ar-Ar ages that are interpreted to reflect the development of S₂ in the region at 440–435 Ma, consistent with late stage Benambran Orogeny. Fitzherbert and Huang

(2019) presented U-Pb dating of hydrothermal titanite from a mineralised D₃ shear zone from Avoca Tank prospect. The hydrothermal titanite gave a robust age of 430 ± 6 Ma, which is consistent with termination of the Benambran Orogeny, collapse of the Girilambone terrane and the onset of Siluro-Devonian back arc spreading. D₄ remains undated but is consistent with deformation related to the ca. 390–380 Ma Tabberabberan Orogeny in the region.

Ore mineralogy and alteration characteristics

D₃ shear hosted mineralisation within metasedimentary sequences at Avoca Tank displays a consistent early oxide

to sulfide-rich paragenesis (Fig. 3). External to the mineralised interval D₃ shear zones display a mineralogy dominated by Fe-rich chlorite and white mica with local magnetite and fine-grained titanite/allanite concentrations. Fine-grained spessartine garnet is locally abundant and maybe associated with magnetite.

Within the mineralised interval, D₃ shear bands preserve an initial ‘oxide phase’ assemblage rich in magnetite, Fe-rich chlorite and quartz (Fig. 3a, b). Both allanite and titanite may be locally abundant in association with the oxide phase. The subsequent ‘sulfide phase’ is reflected initially by the crystallisation and partial replacement of magnetite by pyrite and then chalcopyrite within the earlier formed shears

Fig. 3 Textural relationships of magnetite to sulfides within the Avoca Tank orebody. **a** and **b** Reflected light images of magnetite with siderite and chalcopyrite replacement within a D₃ shear zone. **a** is weakly siderite replaced magnetite on one side of the shear. **b** is strongly siderite replaced magnetite associated with chalcopyrite. **c** Reflected light image of pyrite partially replacing magnetite with a D₃ shear zone. **d** Reflected light image of D₃ magnetite, surrounded by and partially replaced by chalcopyrite. **e** and **f** Pair of plane polarised and reflected light images of D₃ shear hosted magnetite and pyrite (red dashed line) cross cut by a zone of coarser-grained pyrite and chalcopyrite (blue dashed line). **g** Reflected light image of coarse-grained D₃ magnetite surrounded by aggregates of finer-grained euhedral magnetite with both pyrite and chalcopyrite disease (see closeup image **h** for detail). A large anhedral magnetite grain (Mag₁) is recrystallised and partially replaced by the sulfide phase fluid while the finer-grained euhedral magnetite (Mag₂) is in textural equilibrium with chalcopyrite. Red box signifies the location of the closeup image **h**

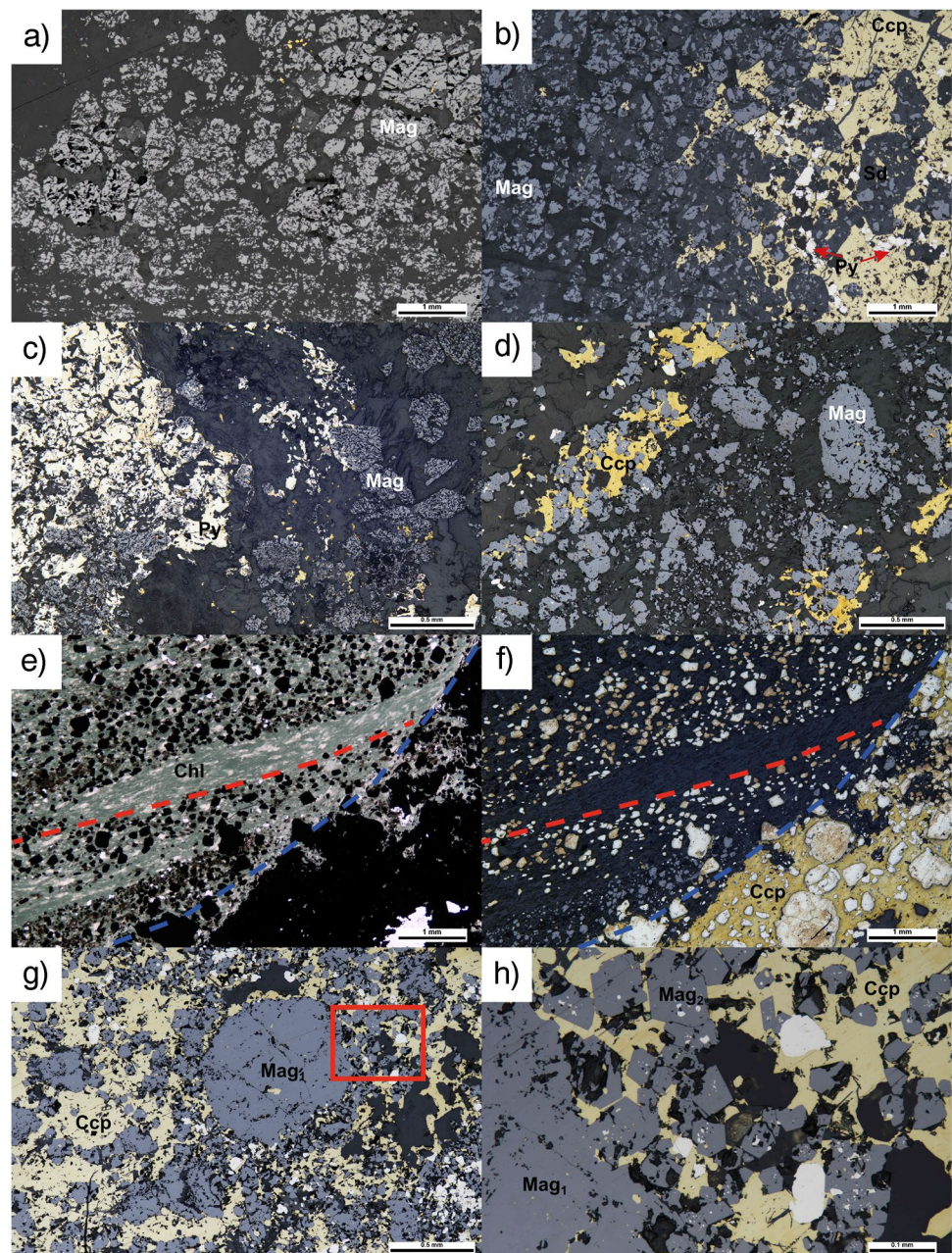


(Fig. 3c, f). Fine blebs of pyrite and chalcopyrite are often present within partially replaced magnetite and pyrite grains (Fig. 3g, h). Within the ore grade shears relic ‘oxide phase’ magnetite are anhedral and recrystallised while magnetite in equilibrium with the ‘sulfide phase’ are smaller and euhedral (Fig. 3h). Chalcopyrite \pm pyrrhotite, low-Fe sphalerite may be locally abundant interstitial to and partially replacing magnetite and pyrite (Fig. 3b, d, e, f, g, h). Sulfide phase gangue mineralogy is dominated by Fe-chlorite, carbonate (including siderite), quartz and stilpnomelane; siderite is mostly present as a partial replacement magnetite in association with the sulfide phase (Fig. 3b). Albite, K-feldspar and white mica may be locally abundant in the ore.

The effects of alteration peripheral to the mineralised D_3 shears diminishes over a short distance (≤ 10 m), often with Fe-rich chlorite, fine-grained magnetite and carbonate invading the S_2 cleavage in the wall rock on a centimetre to decimetre scale. Narrow magnetite-bearing but sulfide barren D_3 shears may also be abundant (over ~ 10 m) within the wall rock in the vicinity of wider, mineralised D_3 shears (Fig. 2). Although the mafic lithologies contain little mineralisation, intense D_3 shearing around the margins of the bodies is associated with strong epidote and carbonate alteration within the mafic bodies themselves and the adjacent metasedimentary rocks.

Analytical methods

The mappable alteration footprint around the Avoca Tank orebody is highly restricted and is characterised with the use of hyperspectral core imaging. Diamond drill holes TATD030 and TATD043 from Avoca Tank were scanned using the HyLogger-3TM instrument at the W.B. Clarke Geoscience Centre, Londonderry, NSW. The HyLogger-3TM is a hyperspectral drill core line profiling instrument that acquires VNIR-SWIR (380–2500 nm) and TIR (6000–14,500 nm) spectra and is co-registered with high-resolution imagery. Spectra collected in the VNIR-SWIR range can be used to detect iron oxides, rare earth minerals, hydrous silicates, carbonates and some sulfates. Variation in key absorption features for chlorite and white mica directly correlates with compositional change, i.e. variation in the ‘2250 nm absorption feature’ reflects changes in the ratio of Mg (lower wavelengths reflect increasing Mg/Fe) and Fe (high wavelengths reflect increasing Fe/Mg) in chlorite-rich spectra, while variation in the ‘2200 nm wavelength feature’ reflects changes in Al abundance within white micas, with lower wavelengths reflecting phengitic compositions and higher wave lengths reflecting muscovitic compositions. Spectra collected from the TIR range can be used to detect anhydrous silicates, carbonates and sulfates and can also be used for identifying hydrous silicates (Schodlok et al. 2016).

One-metre intervals from across the orebody ($n = 5177$) were submitted to ALS Orange for whole-rock multi-element geochemistry by Aeris Resources. Samples were sorted and dried before being crushed and pulverised in preparation for dissolution via a 1:3 ratio of nitric and hydrochloric acid (aqua regia). Major and trace elements were collected using inductively coupled plasma atomic emission spectroscopy (ICP-AES). Accuracy was better than 2% for major elements and 10% for trace elements. Precision was better than 10%. Duplicates were run to validate the data with an accepted variance of up to 3.5% from the duplicated analysis.

Laser ablation inductively coupled plasma mass spectrometry (LA-ICP-MS) mineral analyses for magnetite, pyrite, chalcopyrite and siderite were collected using a Photon Machines Analyte.G2 193 nm ArF Excimer laser ablation system connected to a Thermo iCAP-TQ ICP-MS housed at the Advanced Analytical Centre of James Cook University, Australia. Samples were selected from magnetite-chlorite-quartz assemblages distal to the orebody as well as within the orebody associated with magnetite-pyrite-chalcopyrite-quartz-carbonate. Data collection used the procedures and operating conditions outlined in Petrus et al. (2017) and data reduction was achieved using the Iolite software package (Paton et al. 2011; Paul et al. 2012). Precision was 10% or better for Al, Co, Mn, Ni, Ti and Zn, 15% or better for Mg and V and 20% or better for As, Bi, Cr, Ga, Sb and Sn. For Au, Ca and Cu, precision was better than 30%.

Electron microprobe (EPMA) analyses of chlorite samples were collected using a Cameca SX-100 Camebax Electron Probe Microanalyser at the Centre for Advanced Microscopy located at the Australian National University, Canberra. Analyses were collected using 5 μm beam diameter at an accelerating voltage of 15 kV and a beam current of 15 nA. Chlorite samples were analysed from polished thin sections taken from drill core intervals both proximal and distal to the orebody. Counting times for all analytes was 30 s on peak \pm 15 s on both off peak positions. The matrix correction method was ZAF. Precision and accuracy were better than 2% and 5% respectively for elements over 10 wt% and better than 5% and 10% for minor elements below 1 wt%.

Results

Hyperspectral data and alteration footprint

TATD030

Drill hole TATD030 intersected the main mineralised zone with SWIR data producing an aspectral response due to the high sulfide content (138–143 m; 5 m @ 16.83 wt% Cu, 2.66 g/t Au) and corresponds to a magnetic high (Fig. 4). Downhole SWIR data shows strong variations in white mica and chlorite

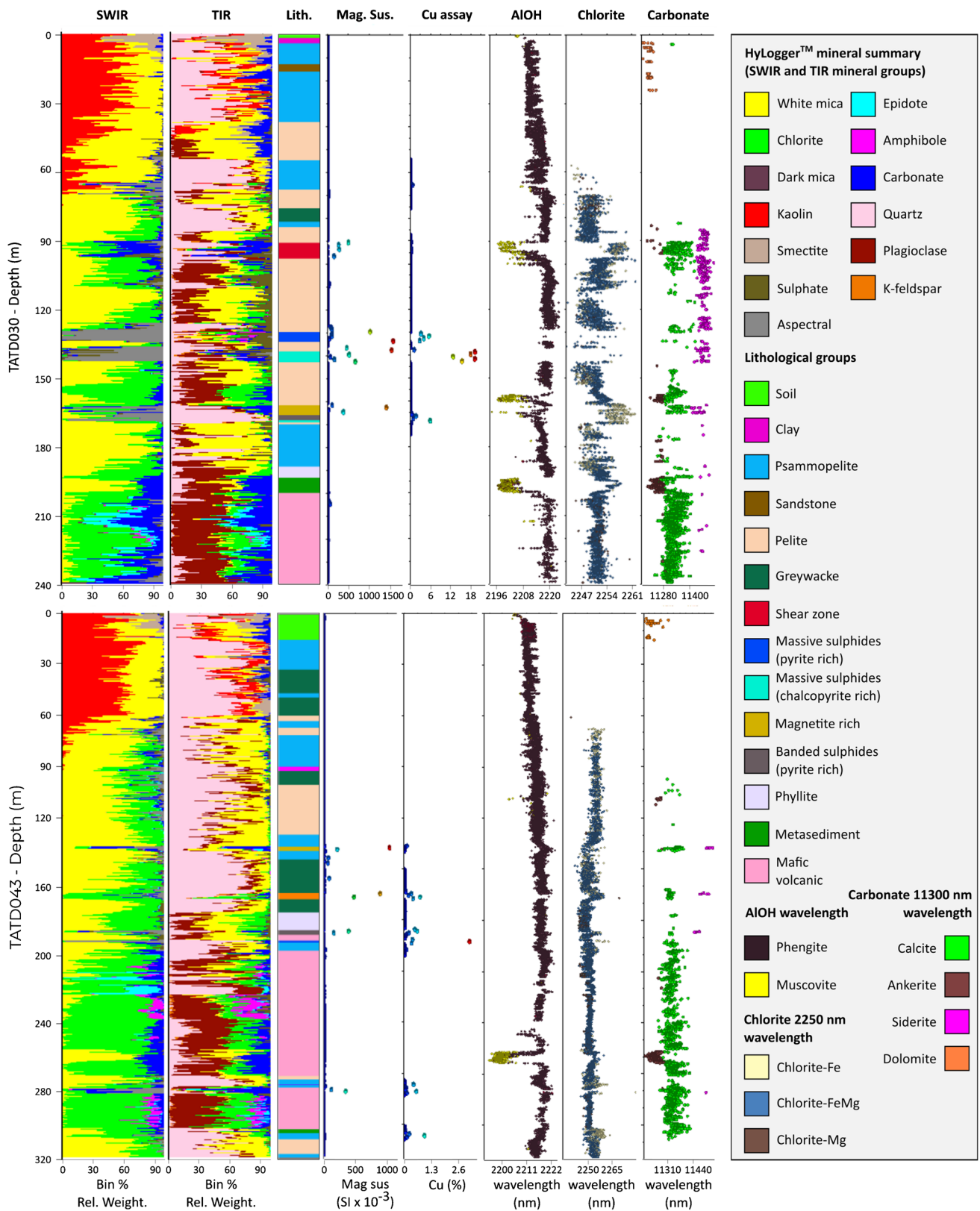


Fig. 4 Drill holes TATD030 and TATD043 HyLogger-3™ SWIR (uTSAS) and TIR (uJCLST) mineralogy plotted against lithology, magnetic susceptibility, Cu assay, AIOH (2200 nm) white mica wavelength, chlorite 2250 nm wavelength and carbonate 11,300 nm wavelength

abundances and can be largely correlated with lithological changes, however also appears to vary systematically with proximity to mineralised shears. Chlorite-FeMg (compositions between Fe-rich and Mg-rich) alteration increases in the hanging wall pelitic lithologies approaching the highest grade shear zone (130–143 m) and trends towards more Fe-rich varieties proximal (within 10 m) to mineralisation (Fig. 4). The reverse trend is observed directly below mineralisation, with chlorite-FeMg decreasing and phengite abundance increasing for ~10 m into the footwall pelite. Similarly, the lower mineralised shear zone shows an increase in chlorite-FeMg abundance and trends towards Fe-chlorite in the hanging wall approaching mineralisation over approximately 12 m. Directly below mineralisation phengite increases in abundance, however the base of the shear zone contacts the psammopelite so it is difficult to discriminate between hydrothermal alteration and lithological change here. TIR data from both mineralised intervals shows that alteration is albite destructive and quartz productive within narrow halos of pervasive silicification localised to mineralised shear zones. Notably, alteration mineralogy in the upper unmineralised shear zone displays a different SWIR signature with abundant chlorite-FeMg and phengite found proximal in both the hanging wall and footwall, and chlorite-Fe, carbonate and muscovite in the shear zone. Unfortunately, this relationship was unable to be confirmed in the lower mineralised shear zones due to the spectral SWIR response; however, no variation in white mica AIOH wavelength (2200 nm) is displayed on the shear zone peripheries. Widespread siderite alteration is found irregularly distributed from the upper unmineralised shear to the lower mineralised shears, while ankerite is found as both lithologically controlled and associated with changes from phengite to muscovite. Below the mineralised intervals, the drill hole intersects mafic volcanic rocks, with alteration involving chlorite + carbonate + epidote \pm actinolite-rich assemblages.

TATD043

Drill hole TATD043 was drilled approximately 70 m north-east of TATD030 and intersected lower grade mineralisation (191–193 m; 3 m @ 1.29 wt% Cu, 0.385 g/t Au) away from the main orebody. Downhole SWIR data shows similar white mica and chlorite variation with changing lithology while alteration here represents a more distal signature and displays similar systematic variations with proximity to mineralisation (Fig. 4). Increased chlorite-FeMg abundance can be observed in the hanging wall approaching the highest grade shear zone for approximately 10 m into the wall rocks and shows similar changes to Fe-rich varieties with proximity to mineralisation. Phengite appears to increase in the footwall immediately below mineralisation for ~3 m into the wall rock; however, the base of the shear zone contacts metasediments so discrimination between lithological change and alteration is difficult.

Two smaller mineralised intervals deeper in the hole (between 280 and 309 m) flank the margins of a mafic sill and display similar trends of increased chlorite-Fe abundance and slightly elevated phengite associated with mineralisation. Systematic albite destruction is consistently observed within mineralised shear zones while local silicification is shown as most intense with increasing Cu grades. Siderite alteration in this drill hole is observed as less intense with only small patches constrained to mineralised shears while ankerite is again observed in association with changes from phengite to muscovite.

Whole rock geochemistry

Whole rock data is presented as bivariate plots against Cu wt% (Fig. 5). As aqua regia is an incomplete digestion technique and some mineral phases will mostly resist digestion, silicate minerals may only undergo slight to moderate dissolution while sulfides and oxides will generally undergo near complete dissolution. Due to the partial dissolution of some minerals, the whole rock data is best considered as semi-quantitative, and identified whole-rock geochemical trends have been validated by quantitative LA-ICP-MS mineral analyses presented below.

We group the data here based on four protoliths: (1) mafic, (2) psammite/greywacke, (3) pelite/psammopelite and (4) unknown. The term ‘unknown’ is used to describe all samples where the protolith is unclear due to alteration or mineralisation. Because the alteration footprint at Avoca Tank is small, the unknown samples can be considered as a proxy for the ore zone itself. Relative to the meta-sedimentary protoliths, the mafic protoliths are enriched in Ca, Al, Cr, Co, Mg, Mn, Ni, V and Ti, while being depleted in P and Zn.

Here, we consider geochemical trends as Cu abundance increases within the orebody. Mineralisation is hosted within sedimentary protoliths with the highest Cu grades observed in the heavily altered intervals. Two trends are identified based on their variation with Cu abundance. The first trend gradually increases elemental concentration as Cu grade increases (Ag, Au, Bi, Fe, Mo, Pb and Zn), while the second trend is either a sharp enrichment or depletion of elements after Cu grade exceeds 2% (As, Co and V enrich while Al, Cr, Mg, Mn, Ni, Sc and Sr deplete). These whole rock trends are mimicked in the paragenetically constrained magnetite and sulfide trace element chemistry.

Trace element characteristics of magnetite

Magnetite-bearing shear zones are distributed throughout the mineralised interval and into the barren hanging wall sequences at Avoca Tank. As a result, magnetite is an ideal target mineral to map mineral chemical change with proximity to mineralisation. Magnetite trace element data is

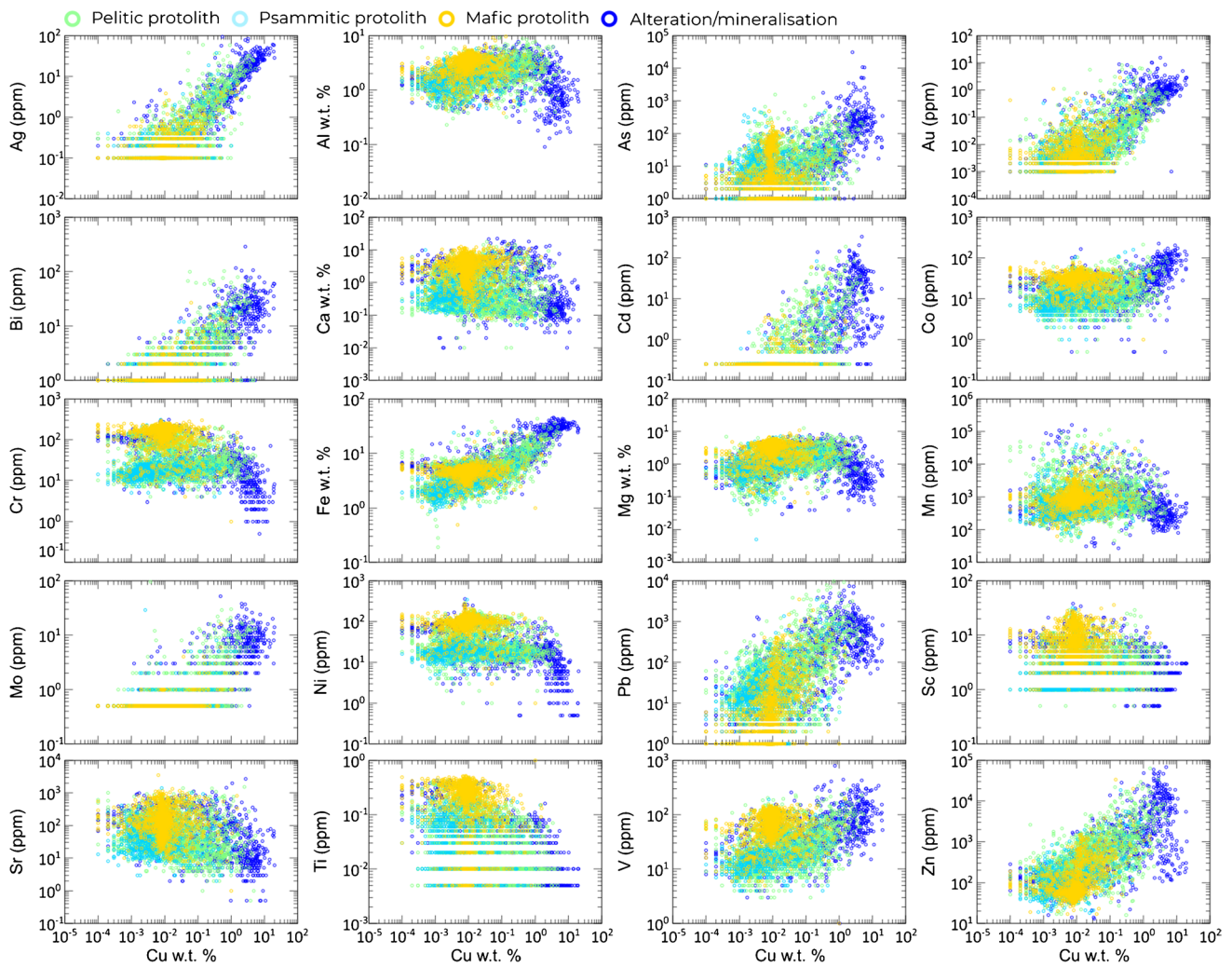


Fig. 5 Whole rock geochemical compositions of Avoca Tank drill core, sampled from across the orebody ($n = 5177$). Major and trace elements are plotted against increasing Cu grade (%) which is used

to indicate proximity to grade. The concentration of economic metals increases consistently with grade; however, the alteration footprint is characterised by rapid changes at Cu grades $>2\%$

presented in ESM Table S1. The trace element characteristics of magnetite are described below in terms of deposit-scale chemical variation and grain-scale trace element zonation. We consider the use of magnetite trace element chemistry as a proximity indicator to Cu mineralisation at Avoca Tank, as well as its use in the discrimination or determination of deposit genesis.

The trace element characteristics of magnetite from Avoca Tank are presented here as multi-element variation diagrams normalised to bulk continental crust (Fig. 6) and box and whisker plots (Fig. 7). Multi-element variation diagrams reflect magnetite analyses from core intersections through magnetite-rich D_3 shears. These are grouped as (i) unmineralised ($<0.1\%$ Cu); (ii) low-grade ($0.1\text{--}1.0\%$ Cu); (iii) moderate-grade ($1.0\text{--}5.0\%$ Cu) and (iv) high-grade ($>5.0\%$ Cu). Drill hole locations, sampling intervals and Cu abundance are shown in ESM Table S2.

Most elements are depleted relative to bulk continental crust (Fig. 6). V is elevated in all samples and overlaps with the high-temperature hydrothermal zone indicated in Fig. 6, which is associated with a coupled depletion in Co and Ni. This feature becomes prominent in the low-grade magnetite samples and both Co and Ni progressively develop into significant negative anomalies with respect to V in the highest-grade ore samples. Ni exhibits this depletion trend in all samples, but some samples show only minor depletion in Co, even within high-grade Cu zones.

Magnetite trace element composition shows distinct variability with increasing Cu grade (Fig. 7). Here, magnetite analyses from the four grade categories are shown as box and whisker plots. As, Bi, Sb and Sn are present in relatively low abundance but are enriched in magnetite from samples with high Cu assays relative to magnetite from unmineralised samples. Zn displays gradual

depletion (although remains relatively abundant) with increasing Cu grade. Co and Ni are depleted in all mineralised samples while abundant in unmineralised samples. Ti is distinctively depleted in the highest-grade zones, while V is enriched.

A selection of LA-ICPMS magnetite trace element maps sampled from high-grade TATD003 and TATD030 depicts the partial recrystallisation of some magnetite in the ore zone, with V depleted and Al, Mn enriched ‘relic’ cores being replaced by V enriched magnetite rims during the sulfide phase (Fig. 8). These textural relationships are consistent with re-equilibration of early formed magnetite during the sulfide phase.

Trace element characteristics of sulfide and carbonate

Pyrite and chalcopyrite are the main sulfide phases that overprint magnetite-rich D_3 shear zones, while siderite replaces magnetite in association with sulfides in many samples (Fig. 3). Where present, pyrite, chalcopyrite and siderite in association with magnetite were analysed.

Fig. 7 Box and whisker plot of Avoca Tank magnetite, pyrite and chalcopyrite trace element compositions according to grade. Here, the horizontal line within the box indicates the median value, while the cross indicates the mean. The box depicts the upper and lower bound for the 1st to 3rd quartile, with the minimum and maximum values are shown as whiskers above and below. Outliers are shown here as dots above each box and whisker

Pyrite

The trace element abundances in pyrite display significant variation with Cu grade and as such are best displayed on box and whisker plots (Fig. 7). It should be noted that issues with micro- to nano-scale chalcopyrite replacement in some pyrite from Avoca Tank makes determination of the true Cu abundance in pyrite and magnetite difficult, especially in samples taken from zone of high Cu whole rock assays. We have deleted all analyses that we believe show evidence of contamination through ablation of chalcopyrite associated with the partial replacement of pyrite or magnetite. Zn is generally below detection limits.

Pyrite from low-grade zones display moderately elevated Co (Avg = 184.5 ppm), Ni (Avg = 105.1 ppm), Ti (Avg = 54.9 ppm), moderate As (Avg = 79.6 ppm) and low Sb

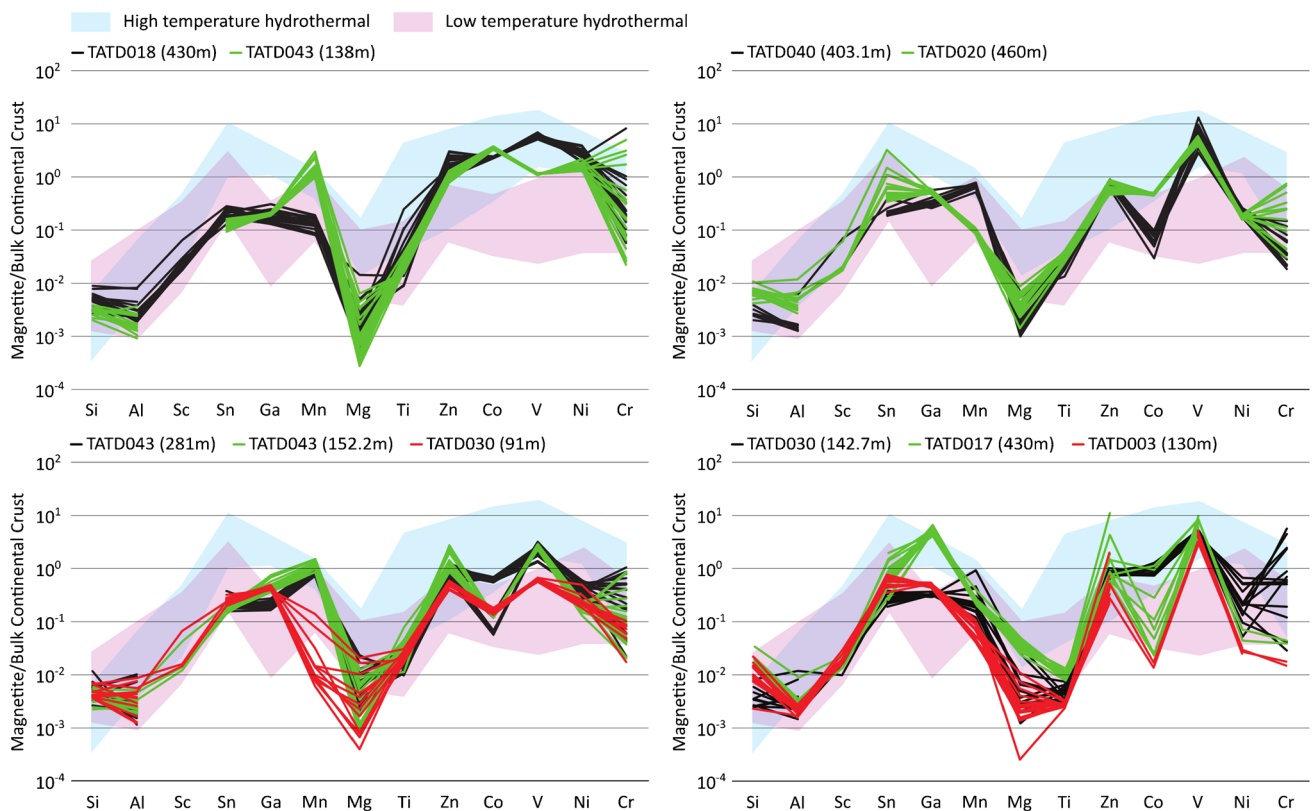
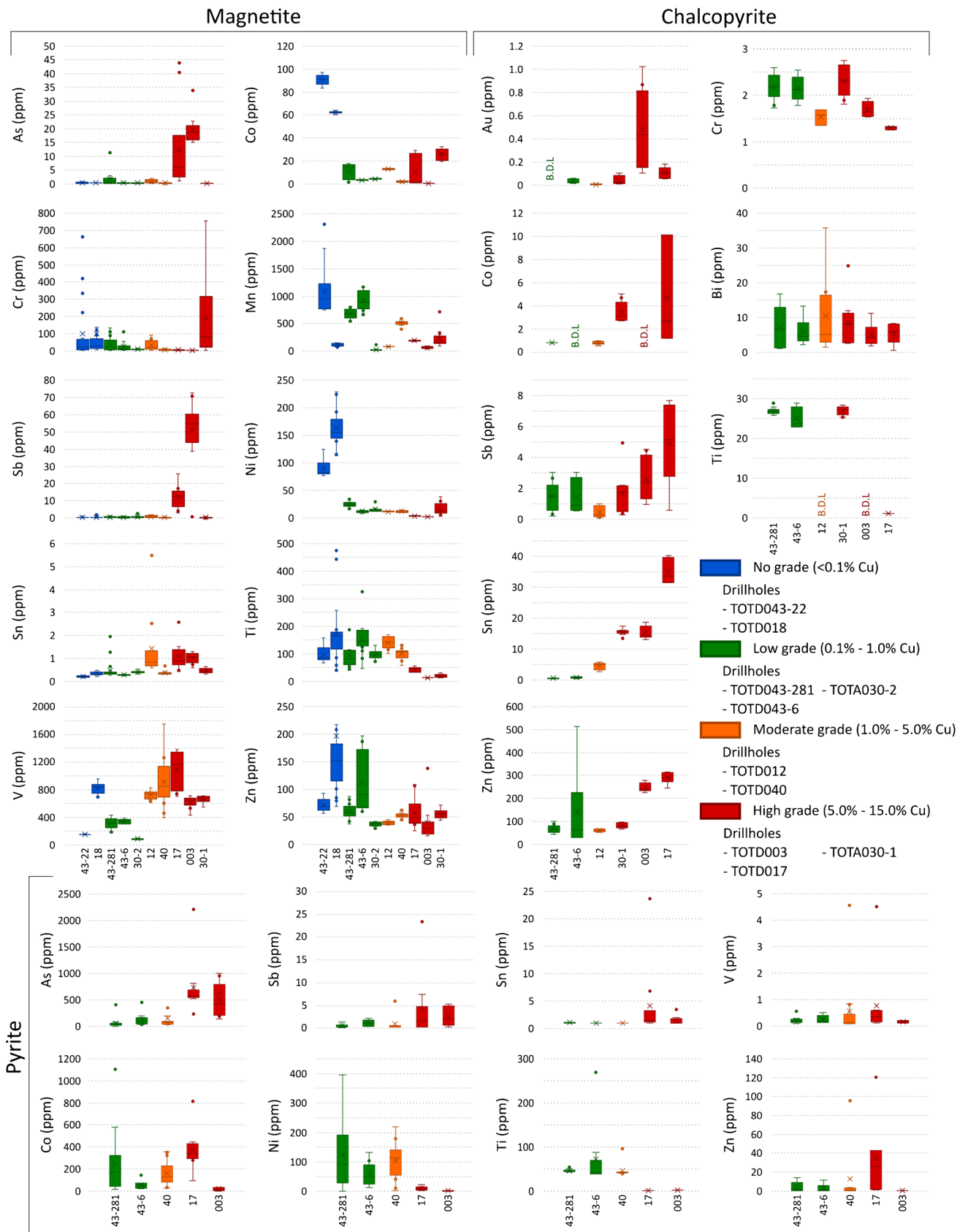


Fig. 6 Magnetite mineral composition multi-element spidergrams normalised to average continental crust values taken from Rudnick and Gao (2003). Data from Avoca Tank magnetite are plotted against hydrothermal magnetite (after Dare et al. 2014)



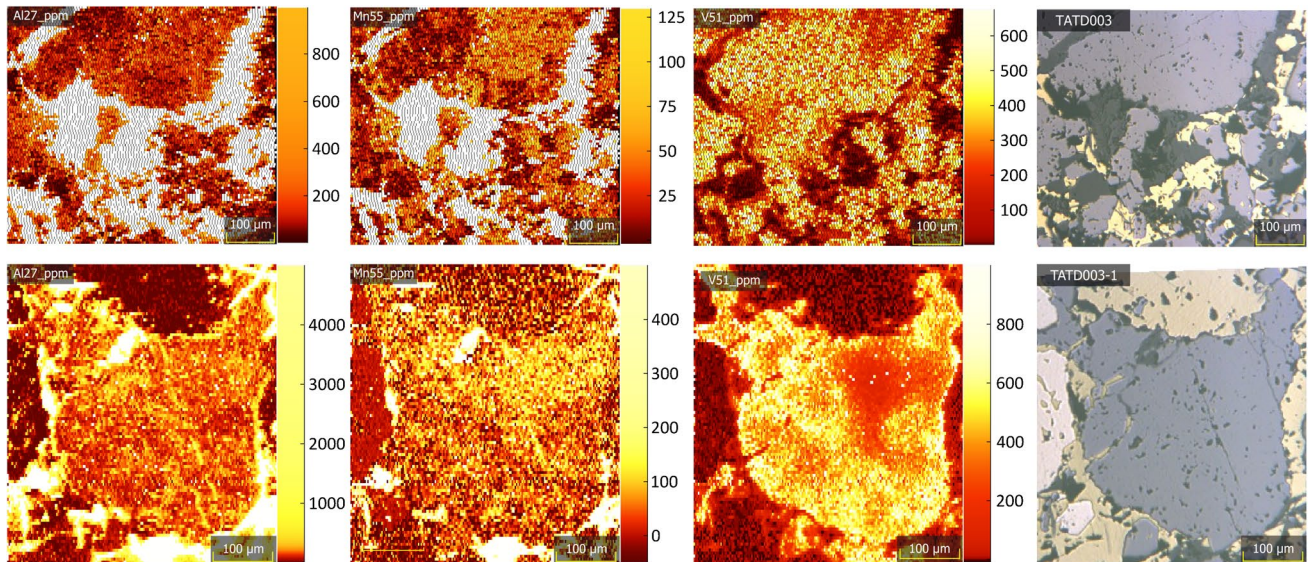


Fig. 8 Quantitative LA-ICP-MS trace element maps of two partially recrystallised magnetite grains sampled from TATD003, within the high-grade zone. Relic magnetite cores enriched in Mn and moderately enriched in Al are incompletely replaced by subsequent V-rich magnetite

(Avg = 0.5 ppm), Sn (0.15 ppm) and V (Avg = 0.24 ppm). Significant changes in elemental abundance occur between low/moderate-grade and high-grade drill core intercepts. Arsenic (Avg = 623.3 ppm) and Co (Avg = 205.9 ppm) display the greatest enrichment in high-grade zones, while Ti (B.D.L. except two analyses) and Ni (Avg = 6.0 ppm) display strong relative depletion. Sn and Sb display similar magnitude enrichment as As (Fig. 7) in high-grade intervals.

Chalcopyrite

Although chalcopyrite is generally considered the least preferred host for a range of trace elements, the trace element abundances in chalcopyrite from Avoca Tank display variation in conjunction with changing whole rock Cu assay (Fig. 7). Chalcopyrite from zones of low whole rock Cu assay displays low abundances of most trace elements, with the exception of Ti (Avg = 26.2 ppm) and Zn (94.5 ppm).

Much like pyrite, little change in elemental abundance is observed between chalcopyrite from low- and moderate-grade Cu zones. Significant changes in elemental abundance occur between low/moderate-grade and high-grade whole rock Cu assays. Enrichments include Zn (Avg = 192.8 ppm), Sn (20.6 ppm) and to a lesser degree in Sb (Avg = 1.5 ppm) and Co (3.8 ppm). Titanium and to a lesser degree Cr are depleted in chalcopyrite from samples from zones of high whole rock Cu assay. Nickel, Cr and V are all in low abundance and display no change in abundance with Cu grade. These trends suggest chalcopyrite likely crystallised without having to compete for trace elements with pyrite or sphalerite, consistent with the paragenesis described for the orebody (George et al. 2018).

Siderite

A small number of siderite analyses were obtained from a low-grade and a high-grade sample. Siderite occurs as a replacement after magnetite and occurs paragenetically alongside galena and or sphalerite. Changes in elemental abundance between low- and high-grade samples involve enrichment in Ti, V, Cr and Cu with depletion in Co, Ni and Zn. Most of these trends mimic those of the magnetite that is being replaced, although the magnitude of Zn depletion may reflect competition with coprecipitating sphalerite.

Chlorite thermometry

Chlorite is brunsvigite in low-grade D₃ shears and ripidolite to brunsvigite in the high-grade shear system according to the classification scheme of Hey (1954). Given the difficulties of stoichiometric recalculation of Fe³⁺ from electron microprobe data in hydrous, halogen-bearing minerals like chlorite, we used the $\Sigma\text{Fe} = \text{Fe}^{2+}$ geothermometer (equation 40) of Lanari et al. (2014). Temperature estimates for the formation of chlorite in the low-grade ore zone are $T_{\text{average}} = 274\text{ }^{\circ}\text{C}$ ($n = 10$) @ 3 kbar and $T_{\text{average}} = 286\text{ }^{\circ}\text{C}$ ($n = 6$) @ 4 kbar, while temperature estimates for the formation of chlorite in the high-grade ore zone are $T_{\text{average}} = 331\text{ }^{\circ}\text{C}$ ($n = 10$) @ 3 kbar and $T_{\text{average}} = 344\text{ }^{\circ}\text{C}$ ($n = 10$) @ 4 kbar (ESM Table 3). These temperatures are consistent with temperature estimates for greenschist facies chlorite-stilpnomelane (predominantly biotite absent) mineral associations (e.g. Lopez-Montano 1984; Thorne et al. 2014; Elmer et al. 2008; Bushmin and Glebovitsky 2008).

Discussion

Changing whole rock geochemistry versus mineral trace element abundances

Whole rock geochemical variation at Avoca Tank varies in relation to increasing Cu grade and several potential geochemical vectors identified that may aid in future exploration for Girilambone Group Cu deposits. Two groups of elements were identified in the whole rock data (Fig. 5); group 1 elements (Au, Bi, Fe, Pb, Zn) increased steadily as Cu grade increased, while group 2 elements experienced a significant shift—either enrichment (As, Co and V) or depletion (Al, Ca, Cr, Mg, Mn, Ni, Sc, Sr and Ti)—in the whole rock data once Cu grade exceeds 2%. The mineral analyses mirror these trends, e.g. where Ni is depleted in the whole rock data once Cu exceeds 2% it is also depleted in the magnetite and sulfide analyses indicating that the pre-existing mineral assemblage has been heavily replaced by new magnetite and sulfides.

Whole rock analyses for Co, Ni, Cr and Ti are relatively enriched in the host sequences and become strongly depleted within the mineralised intervals. Primarily, these elements are hosted in magnetite within the barren shear zones. Within the ore zone, these elements are depleted in the mineral assemblage. This coupled decrease in whole rock and mineral trace element abundances suggests that the later sulfide-rich fluids were depleted in these elements or remained in solution during mineralisation. Therefore, the depletion in whole rock composition can be explained by either the mobilisation of these elements from the system during the sulfide phase or extreme dilution of barren magnetite and replacement with the oxide-sulfide-quartz ore assemblage.

Selective mobility of some transition metals such as Ni likely reflects their solubility in reduced, acidic and hot (>250 °C) hydrothermal fluids (Jansson and Liu 2020). The lack of change in the whole-rock element abundances until very high Cu grades suggests that elemental leaching was confined to the mineralised shear system, with these elements remaining in solution until the hydrothermal fluid experienced significant temperature and/or pH change elsewhere. Within the ore zone mineral assemblages, white mica is exclusively muscovite (Fig. 4) which indicates the presence of an acidic mineralising fluid (Halley et al. 2015). High field strength element mobility in hydrothermal systems is well documented and is dependent on pressure, temperature and pH boundary conditions (Salvi et al. 2000; Jiang et al. 2005; Agangi et al. 2010; Yin et al. 2018). Due to the narrow, metre-scale alteration halo around the mineralised shears, any remobilisation of elements out of the system during mineralisation can have only occurred on a small-scale.

Arsenic, Co and V are enriched in the whole rock data when copper grades exceed 2%. This is mirrored by the mineral analyses for magnetite, pyrite and chalcopyrite and reflects the composition of the sulfide phase fluid. Tin, Sb and Zn increase in concentration within high-grade chalcopyrite; however, the whole rock enrichment of Zn and Sb likely reflects the addition of minor sphalerite into the system. Cobalt displays a decrease in magnetite and minor increase in chalcopyrite as Cu grade increases and is elevated in pyrite. The enrichment in Co in the whole rock data is likely related to increased pyrite abundance. Depletion of Co in magnetite with increasing Cu grade likely reflects re-equilibration with or recrystallisation/co-precipitation with pyrite as magnetite is being replaced by sulfides. Magnetite is notably enriched in V when proximal to the orebody in contrast to magnetite from barren shears.

Other elements that are depleted in the orebody at grades greater than 2% likely reflect dilution in the samples by massive sulfide. Aluminium, K, Sr, Ba and to a lesser extent Ca display depletion with increasing Cu grade, likely reflecting destruction of feldspar in host sedimentary sequences and spatially associated dolerites. This is consistent with hyperspectral logs for TATD030 and TATD043 which show little or no feldspar within the mineralised intervals, as well as the chlorite-quartz-carbonate-rich gangue observed in thin section. Abundance of Ca in the whole rock data is complicated by the addition of some carbonate, often siderite in the mineralised intervals. Mg and to a lesser extent Mn display depletion in the whole rock chemistry with increasing Cu grade and increasing overall modal proportion of sulfide minerals. The hyperspectral data shows a change from Fe-Mg chlorite to Fe-rich chlorite in the gangue mineralogy of the high-grade Cu zones, consistent with chlorite mineral analyses (ESM Table S3). Gangue chlorite also displays an approximate 0.8% depletion in MnO in the high-grade interval. Magnetite (and siderite after magnetite) displays a significant decrease in Mn abundance from low to high Cu grades. Pyrite and chalcopyrite display little change; rare chalcopyrite with elevated Mn is also enriched in elements such as V and Ga that suggest small magnetite inclusions may have been sampled in the analyses. These coupled whole rock and mineralogical depletions suggest that both Mg and Mn remained in solution during the mineralising phase(s) and are depleted in the gangue, oxide and sulfide phases.

The change in As, Co, V, Ni, Sn and Ti in the system is not accounted for by host-rock alteration but rather the abundance of these elements within the primary ore-zone mineral assemblage (chalcopyrite, pyrite and associated magnetite) as Cu grade increases. This makes these elements ideal targets for vectoring towards grade.

Use of magnetite trace element composition as a proximity indicator

Magnetite is associated with most Girilambone Cu deposits, as well as being present in several interpreted exhalative bodies throughout the terrane (Murphy and Cox 2019; Burton et al. 2012). Magnetite-rich zones can be identified remotely through magnetic surveys making magnetite a useful mineral to investigate as a proximity indicator to Cu ore. While common within the terrane, dolerites at Avoca Tank have no discernible magnetic response due to pervasive replacement of primary mineralogy under greenschist facies metamorphism.

Magnetite displays characteristic changes in trace element abundances as Cu grade increases at Avoca Tank. Ni and Co abundance distinguishes magnetite from the unmineralised shear zones from magnetite within shears that host >0.1% Cu. Interestingly, magnetite from unmineralised shear zones displays significant variation in V and Mn between the two samples analysed. These two samples are spatially separated and highlight lateral compositional variation within the unmineralised shear zone. Titanium and to a lesser extent Sn, As and Sb distinguish magnetite from high-grade zones from magnetite in lower grade and unmineralised zones. Elements such as Mn, Sn, V and Zn show potential for separating magnetite composition with progressive increase in Cu grade from low-, moderate- and high-grade zones.

A ternary plot of Ni-V-Ti effectively separates magnetite from unmineralised zones based on Ni abundance, while the ratio of Ti:V effectively separates magnetite from low-, moderate- and high-grade Cu zones (Fig. 9). A ternary plot of (100*Sn)-Zn-Ni discriminates between unmineralised, low-grade and combined moderate- to high-grade zones (Fig. 9). The greatest control here is the ratio of Zn:Sn, but the addition of Ni provides a greater separation between low- versus combined high- and moderate-grade Cu ore. While compositional variation can be depicted on several box and whisker plots and on multi-variant plots, we suggest these ternary diagrams provide a simple and effective visualisation of changing magnetite composition between unmineralised (<0.1% Cu), low-grade (sub-economic <2% Cu) and moderate- to high-grade (economic >2% Cu) mineralisation that could be used to aid exploration in uncovering hidden potential around ‘near miss’ drill holes and potentially as a vector from sub-economic to economic ore at Avoca Tank.

Magnetite and orebody discrimination diagrams

Previous studies detailing the trace element characteristics of magnetite and hydrothermal magnetite (Dupuis and Beaudoin 2011; Dare et al. 2014; Nadoll et al. 2014; Bedard et al.

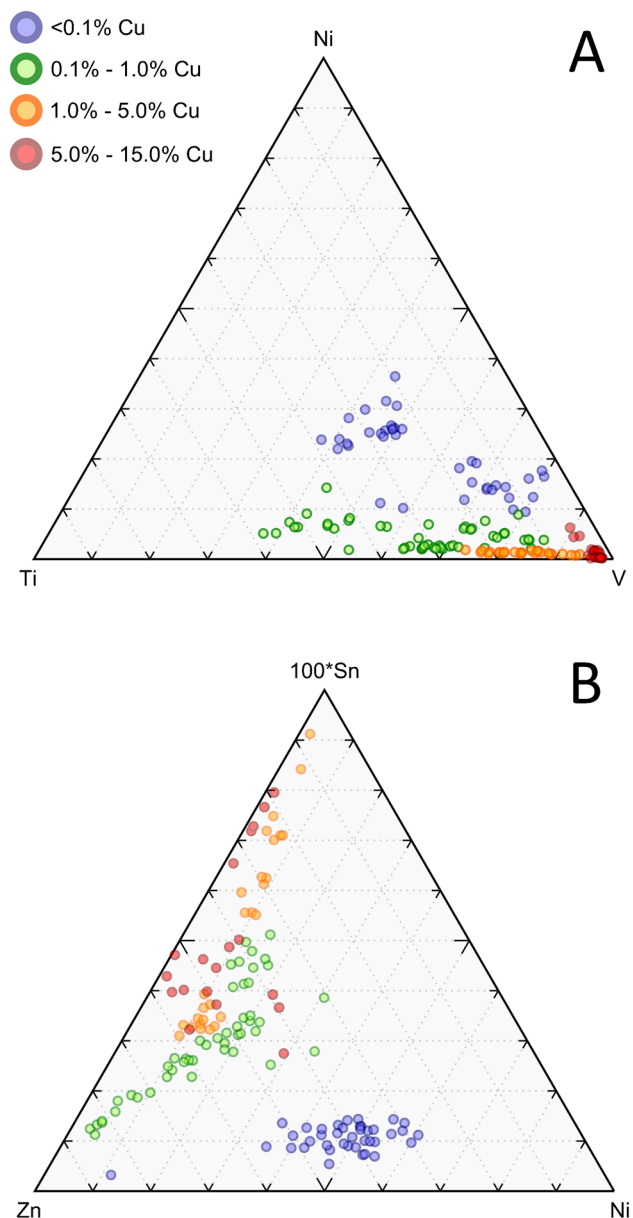


Fig. 9 Ternary vector diagrams. **A** A plot of Ni-V-Ti provides a useful vector from unmineralised magnetite towards magnetite associated with economic grades. **B** A second plot of Sn*100-Zn-Ni effectively separates all ore-related magnetite from those found in barren shears

2022) have provided discrimination methods to predict the style and formation conditions of hydrothermal magnetite-bearing ore bodies. Magnetite from Avoca Tanks is depleted in Ti (and Al) with elevated Ni/Cr ratio attesting to its hydrothermal origins (Dare et al. 2014). Dupuis and Beaudoin (2011) proposed that magnetite from VMS systems can be distinguished in terms of Cu/(Si+Ca) and Al/(Zn+Ca). Magnetite from Avoca Tank is generally depleted in Si, Zn and Ca, plotting compositionally outside the VMS field of

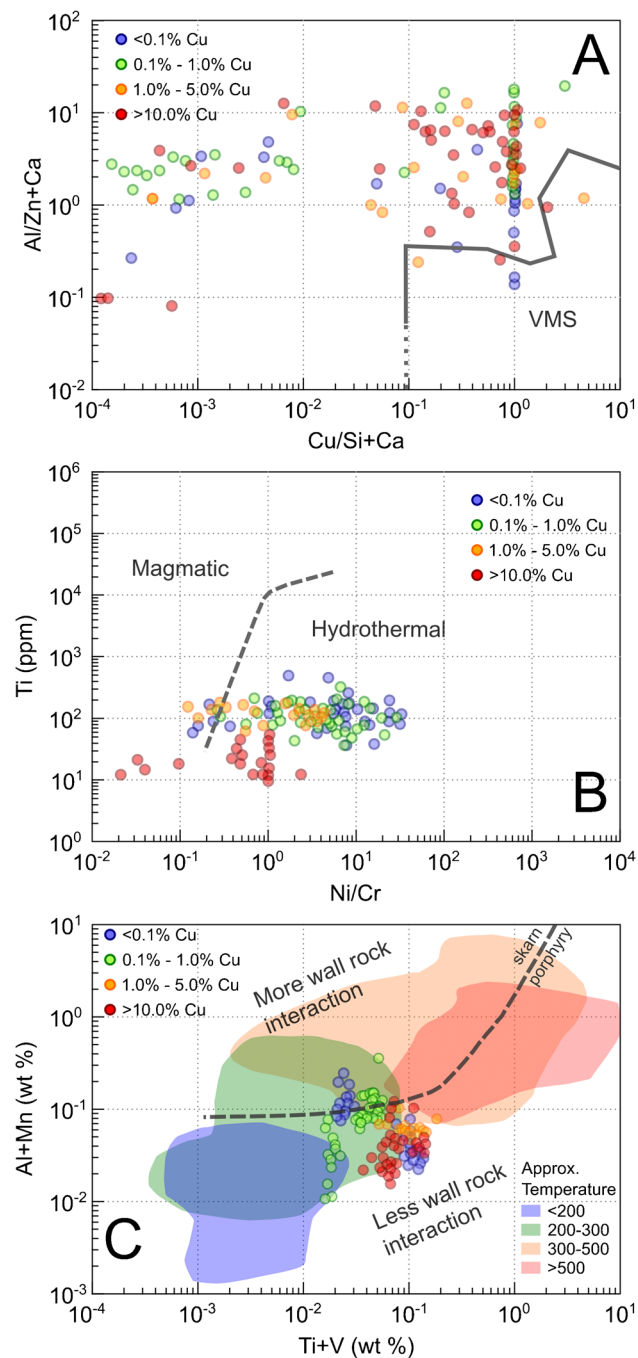


Fig. 10 Magnetite discrimination diagrams after Dare et al. (2014), Dupuis and Beaudoin (2011) and this study based on Nadoll et al. (2014). **A** Avoca Tank magnetite data plotted on an ore deposit discrimination plot after Dupuis and Beaudoin (2011). Data from this study plots outside of the identified VMS field. **B** Avoca Tank magnetite data plotted on a magmatic versus hydrothermal magnetite discrimination plot after Dare et al. (2014). **C** Discrimination made for this study based on Nadoll et al. (2014). Magnetite Al+Mn and Ti+V are used to infer the temperature of the system and the mineralisation style based on the data presented in Nadoll et al. (2014). The skarn vs porphyry dividing line after Nadoll et al. (2014) is included as an indication of wall rock interaction

Dupuis and Beaudoin (2011) (Fig. 10A). Here, data from Avoca Tank forms two rough populations. The first plots adjacent to the VMS field and approximately overlaps with data from skarn, porphyry and IOCG used by Dupuis and Beaudoin (2011). The second group comprises magnetite either depleted in Cu or enriched in Si or Ca and plots to the left and exists outside of the diagram space of the discrimination diagram proposed by these workers. Interestingly, samples from all grade intervals exist in both groups, thus limiting the usefulness of this discrimination plot for our study.

Magnetite from the unmineralised samples has the trace element characteristics of low- to moderate-temperature (300–350 °C) hydrothermal magnetite, being relatively enriched in Ni, V, Co and Zn and depleted in Al and Ti (Figs. 6 and 7) and fits well into the hydrothermal field of Dare et al. (2014) with some minor overlap with the magmatic field (Fig. 10B). This is supported by published data for hydrothermal pyrite which shows good agreement with pyrite mineral analyses at Avoca Tank (Gregory et al. 2019). The overall trends of increasing As, Au, Cu, Sb and Sn in combination with decreasing Ti and Ni relative to increasing whole rock copper assay at Avoca Tank are consistent with low- to moderate-T hydrothermal/metamorphic systems (Gregory et al. 2019). Since the pyrite paragenetically replaces pre-existing magnetite, care needs to be taken in interpreting pyrite chemical trends in isolation as many of the elemental trends mimic and reflect inheritance through scavenging of metals from early formed magnetite (e.g. Steadman and Large 2016), while several of the divergent trends can be explained via elemental compatibility within oxide versus sulfide and relative element solubility within the hydrothermal fluid.

Dupuis and Beaudoin (2011) proposed that Ca+Al+Mn versus Ti+V refined to Al+Mn versus T+V can be used to distinguish between banded iron formation (BIF), iron oxide copper gold (IOCG), skarn and porphyry type magnetite. Magnetite from Avoca Tank displays Ti+V ratios consistent with moderately Ti+V enriched BIF and IOCG-type mineralisation but is depleted in Al+Mn when compared to the data of Dupuis and Beaudoin (2011). Nadoll et al. (2014) suggested that Mn+Al is often related to the degree of wall rock interaction in a mineral system and number of recent publications present magnetite trace element data that is depleted in Al+Mn but has Ti+V values typical of IOCG and porphyry deposits (Spry et al. 2015; Pisiak et al. 2017; Jiao et al. 2019; Wang et al. 2018a, 2018b). As a result, the style of mineralisation which produced the Avoca Tank orebody is unable to be determined from existing discrimination diagrams beyond a broad classification as having a hydrothermal origin after Dare et al. (2014).

To provide additional constraints to mineralisation, we use the coupled change in Al+Mn and Ti+V can be used as a crude magnetite thermometer (Figure 12 in Nadoll et al. 2014). Magnetite from Avoca Tank plots in the low- to moderate-temperature hydrothermal field according to these diagrams, consistent with the chlorite thermometry for the orebody. However, the genetic association of magnetite composition and mineralisation style proposed by Dupuis and Beaudoin (2011) is noted by Nadoll et al. (2014) to poorly correlate with some deposit styles, e.g. BIF and porphyries. We suggest in the light of data presented in this study and recent published data on magnetite trace element composition that temperature fields of Nadoll et al. (2014) can be redrafted to reflect coupled changes in Al+Mn and Ti+V with an emphasis on temperature and degree of wall rock interaction (Fig. 10C).

On such a diagram, magnetite at Avoca Tank formed in a hydrothermal system at moderate temperature (300–350 °C) which is supported by petrographic observations of alteration mineral assemblages and chlorite thermometry. Low Al+Mn suggests limited host rock interaction, which is corroborated by the absence of any extensive alteration halo around the mineralised shears observed in the petrographic and hyperspectral data. Magnetite associated with spessartine garnet-rich shear zones external to the ore may suggest a greater degree of interaction between the Fe-oxide forming fluid and wall rock during fluid transport or sourcing of fluids from an Mn-enriched sequence/source. No genetic inference can be made beyond temperature, degree of wall rock interaction and/or derivation from an Mn-enriched/depleted fluid source.

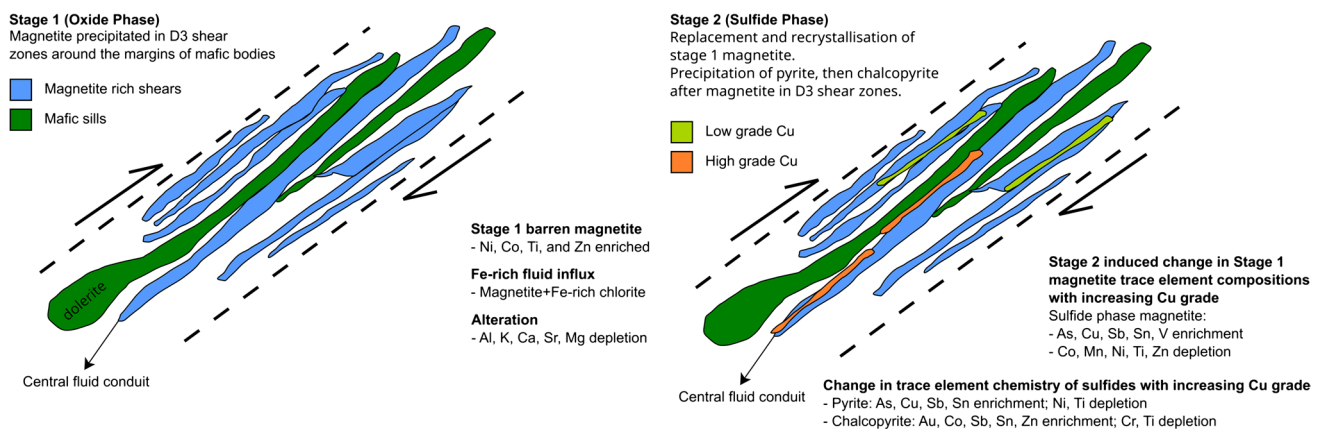


Fig. 11 Ore deposit model for the Avoca Tank prospect. Stage 1 (oxide phase): a hydrothermal fluid is focused within the shear zone along the margins of the dolerite sills (green) forming early-stage barren magnetite within the pre-existing S3 fabric (blue). Stage 2 (sulfide phase): a S-rich fluid is introduced into the system to trigger the resorption and recrystallisation of magnetite as pyrite, chalcopyrite and sphalerite. Initially the sulfides have a similar trace element signature as the destroyed

Magnetite versus sulfide trace element characteristics, inheritance and metamorphic/hydrothermal re-equilibration

Paragenesis involves initial oxide phase magnetite that is partially resorbed during subsequent pyrite crystallisation. Both magnetite and pyrite are further resorbed during chalcopyrite crystallisation and both pyrite and magnetite also display variable replacement by chalcopyrite (Fig. 3). This paragenesis indicates that the mineralising system is zoned temporarily, either due to a single evolving fluid or that the orebody was produced by successive chemically distinct fluids. The chlorite data suggest a temperature increase of ~60 °C between the low-grade margins to the ore system and the high-grade central ore zone. Chlorite crystallises early in the D₃ shear zones, alongside magnetite, while chalcopyrite is associated with an overprinting siderite quartz-rich gangue. This temperature gradient may reflect a zonation within the mineralising system, with the hotter temperatures observed within the central shear system and the cooler temperatures within the wall rocks. Alternatively, the two chlorite compositions may reflect temperature differences between two separate hydrothermal events, e.g. an early barren Fe-rich fluid and later re-equilibration during mineralisation.

While there is good evidence for an early oxide phase which is subsequently overprinted by a sulfide-rich fluid, there is insufficient direct evidence to demonstrate if the orebody was formed by a single evolving fluid or multiple distinct fluid pulses. Therefore, our model for the formation of the Avoca Tank orebody is restricted to characterisation of a stage 1 ‘early’ phase and a stage 2 ‘late’ phase (Fig. 11). Stage 1

magnetite (elevated Cr, Ti and Ni) and evolve to become depleted in these elements and enrich with economic metals (Ag, Au, Bi, Co, Sn, Zn). Where the fluid is either highly focused (e.g. the central fluid conduit) or highly evolved, the alteration is characterised by feldspar destruction and dilution, depleting the system of K, Sr, Ba and some Ca. Chlorite is dominated by Fe-endmembers and the system depleted is Mg and Mn proximal to the ore zone, although some drill holes are Mn-rich

precipitated a barren Fe-rich mineral assemblage dominated by chlorite and magnetite enriched in Co, Mn, Ni, Ti and Zn. These Fe-rich shears then provided a suitably reactive trap for the subsequent sulfide-rich phase enriched in Cu, Sb, Sn and V. Trace element chemistry obtained from magnetite within the high-grade ore zones (Fig. 7) demonstrate significant enrichment of As, Sb and V which is interpreted to represent a distinct change in fluid composition from the earlier stage 1 oxide phase. The extent that the stage 2 sulfide phase fluid adds additional Co and Zn into the system is undetermined. The earliest pyrite dominated sulfide phase has several geochemical characteristics in common with the stage 1 oxide phase (elevated Cr, Ti and Ni) and evolves towards enrichment of Ag, As, Au, Bi, V and Zn.

Magnetite which crystallised during stage 1 is trace element homogenous and distinct from magnetite which has crystallised during stage 2. This requires that either all stage 1 magnetite within the mineralised shears is destroyed during mineralisation or that this magnetite has been recrystallised and has a trace element chemistry which reflects the stage 2 fluid. Textural evidence observed in thin section shows that anhedral and recrystallised stage 1 magnetite is preserved in the ore zone alongside euhedral magnetite in equilibrium with chalcopyrite (Fig. 3g and h). Laser ablation maps of recrystallised magnetite grains from within the high-grade zones show that in some cases magnetite preserve relic cores which have trace element compositions consistent with the earlier oxide phase (Fig. 8). Magnetite within low-grade zones may be partially recrystallised or resist recrystallisation entirely thus preserving the trace element signature of the barren oxide phase fluid. The orebody has a strong structural control and exploits S_3 and sometimes pre-existing S_3 fabrics, commonly along the interface of the mafic sills and the sedimentary host rocks. We suggest the resorption and partial to complete re-equilibration and destruction of stage 1 magnetite is related to hydrothermal mineralisation occurring within a middle greenschist facies metamorphic terrane during the onset of Tabberabberan extension.

Conclusions

Mineralisation at Avoca Tank is contained within in D_3 shear system that formed at ca. 430 Ma following the Benambran Orogen. Mineralisation within these shears developed during greenschist facies conditions with initial magnetite-rich, oxide phase shear zones overprinted by sulfide phase pyrite-chalcopyrite. Copper mineralisation within the Girilambone terrane is associated with Ordovician aged mafic magmatism and although mineralisation at Avoca Tank is epigenetic in nature, being hosted in ca. 430 Ma shear arrays, the Cu metal endowment is described as being related to Ordovician aged back

arc processes. The trace element chemistry of magnetite re-equilibrated under greenschist facies conditions during sulfide mineralisation, forming distinctive deposit-scale trace chemical zonation in magnetite with increasing Cu grade. Variations in Ni-V-Ti and Sn ($100 \times \text{Sn}$)-Zn-Ni effectively distinguish magnetite from unmineralised, low-, moderate- and high-grade Cu zones. These two ternary systems graphically illustrate changing magnetite composition between unmineralised ($<0.1\%$ Cu), low-grade (sub-economic $<2\%$ Cu) and moderate- to high-grade (economic $>2\%$ Cu) mineralisation and therefore could be used to aid in vectoring from sub-economic to economic ore.

Supplementary Information The online version contains supplementary material available at <https://doi.org/10.1007/s00126-023-01204-9>.

Acknowledgements The authors would like to thank David Huston and an anonymous reviewer for their careful, expert and informative reviews that greatly improved both the science and readability of the manuscript. Phillip Blevin is also thanked for commenting on earlier versions of the manuscript. Brenainn Simpson and Joel Fitzherbert publish with the permission of the Executive Director Geological Survey of New South Wales.

Funding Open Access funding enabled and organized by CAUL and its Member Institutions

Declarations

Competing interests The authors declare no competing interests.

Open Access This article is licensed under a Creative Commons Attribution 4.0 International License, which permits use, sharing, adaptation, distribution and reproduction in any medium or format, as long as you give appropriate credit to the original author(s) and the source, provide a link to the Creative Commons licence, and indicate if changes were made. The images or other third party material in this article are included in the article's Creative Commons licence, unless indicated otherwise in a credit line to the material. If material is not included in the article's Creative Commons licence and your intended use is not permitted by statutory regulation or exceeds the permitted use, you will need to obtain permission directly from the copyright holder. To view a copy of this licence, visit <http://creativecommons.org/licenses/by/4.0/>.

References

- Agangi A, Kamenetsky VS, McPhie J (2010) The role of fluorine in the concentration and transport of lithophile trace elements in felsic magmas: insights from the Gawler Range Volcanics, South Australia. *Chem Geol* 273:314–325
- Bedard E, Bronac D, de Vazelhes V, Beaudoin B (2022) Performance of predictive supervised classification models of trace elements in magnetite for mineral exploration. *J Geochem Explor* 236:106959
- Boutroy E, Dare S, Beaudoin G, Barnes SJ, Lightfoot P (2014) Magnetite composition in Ni-Cu-PGE deposits worldwide: application to mineral exploration. *J Geochem Explor* 145
- Brugger J, Lahaye Y, Costa S, Lambert D, Bateman R (2000) Inhomogeneous distribution of REE in scheelite and dynamics of Archaean hydrothermal systems (Mt. Charlotte and Drysdale gold deposits, Western Australia). *Contrib Mineral Petrol* 139:251–264

- Burton GR (2011) Interpretation of whole rock geochemical data for samples of mafic schists from the Tritton area, central New South Wales. Geological Survey of New South Wales Report GS2012/0264, Maitland
- Burton, G.R., Trigg, S.J., and Campbell, L.M. 2012. Sussex and Byrock 1:100 000 geological sheets 8135 and 8136. Explanatory notes. (Maitland, NSW.: Geological Survey of New South Wales).
- Bushmin SA, Glebovitsky VA (2008) Scheme of mineral facies of metamorphic rocks. *Geol Ore Deposits* 50:659–669
- Carew MJ, Mark G, Oliver NHS, Pearson N (2006) Trace element geochemistry of magnetite and pyrite in Fe oxide (\pm Cu–Au) mineralised systems: insights into the geochemistry of ore-forming fluids. *Geochim Cosmochim Acta* 70:A83
- Cooke, D.R., Agnew, P., Hollings, P., Baker, M., Chang, Z., Wilkinson, J.J., White, N.C., Zhang, L., Thompson, J., Gemmill, J.B., et al. 2017. Porphyry indicator minerals (PIMS) and porphyry vectoring and fertility tools (PVFTS) – indicators of mineralization styles and recorders of hypogene geochemical dispersion halos. In Proceedings of exploration 17, V. Tschirhart, and M.D. Thomas, eds. pp. 457–470
- Dare SAS, Barnes S-J, Beaudoin G (2012) Variation in trace element content of magnetite crystallised from a fractionating sulfide liquid, Sudbury, Canada: implications for provenance discrimination. *Geochim Cosmochim Acta* 88:27–50
- Dare SAS, Barnes SJ, Beaudoin G, Méric J, Boutroy E, Potvin-Doucet C (2014) Trace elements in magnetite as petrogenetic indicators. *Miner Deposita* 49:785–796
- Downes PM, Raymond C, Fitzherbert JA (2017) Girilambone copper district. In: Phillips GN (ed) Australian ore deposits. Australasian Institute of Mining and Metallurgy, pp 473–478
- Dupuis C, Beaudoin G (2011) Discriminant diagrams for iron oxide trace element fingerprinting of mineral deposit types. *Miner Deposita* 46:319–335
- Elmer FL, Dugdale AL, Wilson CJL (2008) Application of mineral equilibria modeling to constrain T and X CO₂ conditions during the evolution of the Magdala gold deposit, Stawell, Victoria, Australia. *Miner Deposita* 43:759–776
- Evans GN (2017) Trace element proxies and mineral indicators of hydrothermal fluid composition and seafloor massive sulfide deposit formation processes. Unpublished Doctor of Philosophy, Massachusetts Institute of Technology and the Woods Hole Oceanographic Institution
- Fergusson CL, Henderson RA (2015) Early Palaeozoic continental growth in the Tasmanides of northeast Gondwana and its implications for Rodinia assembly and rifting. *Gondw Res* 28:933–953
- Fitzherbert JA, Downes PM (2020) A mineral system model for Cu–Au–Pb–Zn–Ag systems of the Cobar Basin, central Lachlan Orogen, New South Wales. Geological Survey of New South Wales Report GS2021/0042, Maitland
- Fitzherbert JA, Huang H (2019) U–Pb dating of hydrothermal titanite from the Avoca Tank deposit. Geological Survey of New South Wales, Maitland
- George LL, Cook NJ, Crowe BBP, Ciobanu CL (2018) Trace elements in hydrothermal chalcopyrite. *Mineral Mag* 82:59–88
- Gilmore, P.J. 2014. Exhalative horizons and volcanic-associated massive sulfide (VMS) deposits in the Ordovician Girilambone Group, NSW. Geological Survey of New South Wales (GS2014/0939)
- Gilmore, P.J., Trigg, S.J., and Campbell, L.M. 2018. Coolabah 1:100 000 geological sheet 8235, 1st edition, Explanatory notes. (Maitland, NSW.: Geological Survey of New South Wales)
- Glen RA, Crawford AJ, Percival IG, Barron LM (2007) Early Ordovician development of the Macquarie Arc, Lachlan Orogen, New South Wales. *Aust J Earth Sci* 54:167–179
- Gourcerol B, Kontak DJ, Thurston PC, Duparc Q (2016) Do magnetite layers in Algoma-type banded iron formations (BIF) preserve their primary geochemical signature? A case study of samples from three Archean BIF-hosted gold deposits. *Can Mineral* 54:605–624
- Grant FS (1985) Aeromagnetism, geology and ore environments, I. Magnetite in igneous, sedimentary and metamorphic rocks: an overview. *Geoexploration* 23:303–333
- Gregory DD, Cracknell MJ, Large RR, McGoldrick P, Kuhn S, Maslennikov VV, Baker MJ, Fox N, Belousov I, Figueroa MC et al (2019) Distinguishing ore deposit type and barren sedimentary pyrite using laser ablation-inductively coupled plasma-mass spectrometry trace element data and statistical analysis of large data sets. *Econ Geol* 114:771–786
- Grigsby JD (1990) Detrital magnetite as a provenance indicator. *SEPM J Sediment Res* 60
- Hall JM, Fisher BE (1987) The characteristics and significance of secondary magnetite in a profile through the dike component of the Troodos, Cyprus, ophiolite. *Can J Earth Sci* 24:2141–2159
- Halley S, Dilles JH, Tosdal RM (2015) Footprints: hydrothermal alteration and geochemical dispersion around porphyry copper deposits. *SEG Discov* 2015(100):1–17. <https://doi.org/10.5382/SEGnews.2015-100.fea>
- Heimann A, Spry PG, Teale GS (2005) Zincian spinel associated with metamorphosed Proterozoic base-metal sulfide occurrences, Colorado: a re-evaluation of gahnite composition as a guide in exploration. *Can Mineral* 43:601–622
- Hey MH (1954) A new review of the chlorites. *Mineral Mag J Mineral Soc* 30:277–292
- Hinde, S. 2019. Advances in geological understanding driving exploration in the Girilambone district. Discoveries in the Tasmanides September 2019, Wagga Wagga, New South Wales. <https://smedg.org.au/mw-papers-2019/>
- Huang X-W, Boutroy É, Makvandi S, Beaudoin G, Corriveau L, De Toni AF (2019a) Trace element composition of iron oxides from IOCG and IOA deposits: relationship to hydrothermal alteration and deposit subtypes. *Miner Deposita* 54(4):525–552
- Huang X-W, Sappin A-A, Boutroy É, Beaudoin G, Makvandi S (2019b) Trace element composition of igneous and hydrothermal magnetite from porphyry deposits: relationship to deposit subtypes and magmatic affinity. *Econ Geol* 114(5):917–952
- Huston DL, Champion DC, Mernagh TP, Downes PM, Jones P, Carr G, Forster D, David V (2016) Metallogensis and geodynamics of the Lachlan Orogen: new (and old) insights from spatial and temporal variations in lead isotopes. *Ore Geol Rev* 76:257–267
- Jansson NF, Liu W (2020) Controls on cobalt and nickel distribution in hydrothermal sulphide deposits in Bergslagen, Sweden - constraints from solubility modelling. *GFF* 142:87–95
- Jiang S-Y et al (2005) Mobility of high field strength elements (HFSE) in magmatic-, metamorphic-, and submarine-hydrothermal systems. *Phys Chem Earth Parts ABC* 30(17):1020–1029
- Jiao J, Han F, Zhao L, Duan J, Wang M (2019) Magnetite geochemistry of the Jinchuan Ni–Cu–PGE deposit, NW China: implication for its ore-forming processes. *Minerals* 9:593
- Jones, P. 2012. Tritton copper mine: mineralisation and host sequence. In Post-conference field excursion; geology and mineralisation of the Cobar–Nyngan region. (Geological Survey of New South Wales Report GS2012/695)
- Knipping JL, Bilinker LD, Simon AC, Reich M, Barra F, Deditius AP, Lundstrom C, Bindeman I, Munizaga R (2015) Giant Kiruna-type deposits form by efficient flotation of magmatic magnetite suspensions. *Geology* 43:591–594
- Lanari P, Wagner T, Vidal O (2014) A thermodynamic model for dioctahedral chlorite from experimental and natural data in the system MgO–FeO–Al₂O₃–SiO₂–H₂O. Applications to P–T sections and geothermometry. *Contrib Mineral Petrol* 167:968
- Lawrie CK, Hinman MC (1998) Cobar-style polymetallic Au–Cu–Ag–Pb–Zn deposits. *AGSO J Aust Geol Geophys* 17:169–187
- López-García JA, Oyarzun R, Lillo J, Manteca JL, Cubas P (2017) Geochemical characterization of magnetite and geological setting of the iron oxide \pm iron silicate \pm iron carbonate rich Pb–Zn sulfides from the La Unión and Mazarrón stratabound deposits (SE

- Spain): unusual magnetite-rich Pb-Zn ores from Spain. *Resour Geol* 67:139–157
- Lopez-Montano R (1984) Stilpnomelane and associated minerals in the Hällefors dolerite dyke, south central Sweden. *Geol Fören Stockh Förh* 106:73–79
- Makvandi, S., Beaudoin, G., Ghasemzadeh-Barvarz, M., and McClenaghan, M.B. 2013. Fingerprinting volcanogenic massive sulfide deposits using magnetite chemistry: application to till from Izok Lake, Nunavut, Canada. In 12th SGA biennial meeting, (Uppsala, Sweden)
- Mao M, Rukhlov AS, Rowins SM, Spence J, Coogan LA (2016) Apatite trace element compositions: a robust new tool for mineral exploration. *Econ Geol* 111:1187–1222
- Maskell A, Duuring P, Hagemann SG (2014) Hydrothermal alteration events controlling magnetite-rich iron ore at the Matthew Ridge prospect, Jack Hills greenstone belt, Yilgarn Craton. *Aust J Earth Sci* 61:187–212
- Mavrogenatos C, Voudouris P, Berndt J, Klemme S, Zaccarini F, Spry PG, Melfos V, Tarantola A, Keith M, Klemd R et al (2019) Trace elements in magnetite from the Pagoni Rachi porphyry prospect, NE Greece: implications for ore genesis and exploration. *Minerals* 9:725
- Murphy, T., and Cox, B. 2019. Development in understanding of the Tritton-Girilambone Cu district, Australia; resolving hydrothermal mineralisation in multiply-deformed rocks. In PACRIM 2019, (Auckland).
- Nadoll P (2011) Geochemistry of magnetite from hydrothermal ore deposits and host rocks – case studies from the Proterozoic Belt Supergroup, Cu-Mo-porphyry + skarn and Climax-Mo deposits in the western United States. PhD thesis. University of Auckland
- Nadoll P, Angerer T, Mauk JL, French D, Walshe J (2014) The chemistry of hydrothermal magnetite: a review. *Ore Geol Rev* 61:1–32
- O'Brien JJ, Spry PG, Teale GS, Jackson SE, Koenig AE (2015) Gahnite composition as a means to fingerprint metamorphosed massive sulfide and non-sulfide zinc deposits. *J Geochem Explor* 159:48–61
- Paton C, Hellstrom J, Paul B, Woodhead J, Hergt J (2011) Iolite: freeware for the visualisation and processing of mass spectrometric data. *J Anal At Spectrom.* <https://doi.org/10.1039/c1ja10172b>
- Paul, B., Paton, C., Norris, A., Woodhead, J., Hellstrom, J., Hergt, J., and Greig, A. (2012) CellSpace: a module for creating spatially registered laser ablation images within the Iolite freeware environment. *J Anal At Spectrom.*, v. 27, no. 4, p. 700, doi: <https://doi.org/10.1039/c2ja10383d>
- Petrus JA, Chew DM, Leybourne MI, Kamber BS (2017) A new approach to laser-ablation inductively-coupled-plasma mass-spectrometry (LA-ICP-MS) using the flexible map interrogation tool 'Monocle'. *Chem Geol* 463:76–93
- Pisiak LK, Canil D, Lacourse T, Plouffe A, Ferbey T (2017) Magnetite as an indicator mineral in the exploration of porphyry deposits: a case study in till near the Mount Polley Cu-Au deposit, British Columbia, Canada. *Econ Geol* 112:919–940
- Poulin RS, Kontak DJ, McDonald A, McClenaghan MB (2018) Assessing scheelite as an ore-deposit discriminator using its trace-element and REE. *Can Mineral* 56:265–302
- Razjigaeva NG, Naumova VV (1992) Trace element composition of detrital magnetite from coastal sediments of Northwestern Japan Sea for provenance study. *SEPM J Sediment Res* 62:802–809
- Rudnick RL, Gao S (2003) Composition of the continental crust. In: Rudnick K (ed) *The crust*. Elsevier, UK, p 708
- Salvi S, Fontan F, Monchoux P, Williams-Jones AE, Moine B (2000) Hydrothermal mobilization of high field strength elements in alkaline igneous systems: evidence from the Tamazeght Complex (Morocco). *Econ Geol* 95:559–576
- Schodlok MC, Whitbourn L, Huntington J, Mason P, Green A, Berman M, Coward D, Connor P, Wright W, Jolivet M et al (2016) HyLogger-3, a visible to shortwave and thermal infrared reflectance spectrometer system for drill core logging: functional description. *Aust J Earth Sci* 63:929–940
- Spry, P.G., O'Brien, J.J., Frank, K.S., Teale, G.S., Koenig, A., Jansson, N., Allen, R., and Raat, H. 2015. Trace element compositions of silicates and oxides as exploration guides to metamorphosed massive sulphide deposits: examples from Broken Hill, Australia, and Stollberg, Sweden. In *Application of indicator mineral methods to mineral exploration, short course SC02*, (Tucson)
- Steadman JA, Large RR (2016) Synsedimentary, diagenetic, and metamorphic pyrite, pyrrhotite, and marcasite at the Homestake BIF-hosted gold deposit, South Dakota, USA: insights on Au-As ore genesis from textural and LA-ICP-MS trace element studies. *Econ Geol* 111:1731–1752
- Stegman CL (2001) Cobar deposits: still defying classification! *SEG Discov*:1–60
- Suppel, D.W. 1975. Copper deposits in the Girilambone Beds, Tottenham, New South Wales. (Geological Survey of New South Wales).
- Thorne WS, Hagemann SG, Sepe D, Dalstra HJ, Banks DA (2014) Structural control, hydrothermal alteration zonation, and fluid chemistry of the concealed, high-grade 4EE iron orebody at the Paraburdoo 4E deposit, Hamersley Province, Western Australia. *Econ Geol* 109:1529–1562
- Valvasori AA, Hanchar JM, Piercey SJ, Fonkwe MLD (2020) The origin and evolution of V-rich, magnetite dominated Fe-Ti oxide mineralization; Northwest River Anorthosite, south-central Labrador, Canada. *Miner Deposita* 55:555–575
- Wang C, Shao Y, Zhang X, Dick J, Liu Z (2018a) Trace element geochemistry of magnetite: implications for ore genesis of the Huanggangliang Sn-Fe deposit, Inner Mongolia, Northeastern China. *Minerals* 8:195
- Wang Y, Gao J, Huang X, Qi L, Lyu C (2018b) Trace element composition of magnetite from the Xinqiao Fe-S(-Cu-Au) deposit, Tongling, Eastern China: constraints on fluid evolution and ore genesis. *Acta Geochim* 37:639–654
- Wang Y-J, Zhu W-G, Huang H-Q, Bai Z-J, Zhong H, Yao J-H, Fan H-P (2020) Geochemistry of magnetite from the giant Paleoproterozoic Dahongshan Fe-Cu deposit, SW China: constraints on nature of ore-forming fluids and depositional setting. *Ore Geol Rev* 118:103361
- Wilkinson JJ, Baker MJ, Cooke DR, Wilkinson CC (2020) Exploration targeting in porphyry Cu systems using propylitic mineral chemistry: a case study of the El Teniente deposit, Chile. *Econ Geol* 115:771–791
- Yang S, Wang Z, Guo Y, Li C, Cai J (2009) Heavy mineral compositions of the Changjiang (Yangtze River) sediments and their provenance-tracing implication. *J Asian Earth Sci* 35:56–65
- Yin S, Ma C, Robinson PT (2018) Textures and high field strength elements in hydrothermal magnetite from a skarn system: implications for coupled dissolution-reprecipitation reactions. *Am Mineral*
- Zhao J, Brugger J, Pring A (2019) Mechanism and kinetics of hydrothermal replacement of magnetite by hematite. *Geosci Front* 10:29–41

Publisher's note Springer Nature remains neutral with regard to jurisdictional claims in published maps and institutional affiliations.